Depinning of water droplets from a horizontal solid surface by wall-bounded shear flows

Xueqing Zhang, Jeremy D. Newton, Serhiy Yarusevych, and Sean D. Peterson
Mechanical and Mechatronics Engineering, University of Waterloo, Waterloo, Ontario N2L3G1, Canada

(Received 11 October 2022; accepted 21 December 2023; published 28 March 2024)

The onset of droplet motion along a horizontal anodized aluminum surface arising from aerodynamic loading imposed by an accelerating wall-bounded shear flow was investigated for water droplet volumes ranging from 75 to 120 μL. Two accelerating shear flows were considered, a flat plate boundary layer and an impinging jet with orientation angles spanning 30° to 90°. The flows were linearly accelerated at three different rates, 1.2, 2.2, and 4.4 $\mathrm{m/s^2}$, to a maximum flow speed of 20 m/s. Droplets in the flat plate boundary layer were observed to have a constant depinning threshold Weber number of $\mathrm{We}_{h,\mathrm{crit}} = 7.5 \pm 0.5$. By contrast, droplets in impinging jets exhibited lower thresholds in the range of $2 \lessapprox \mathrm{We}_{h,\mathrm{crit}} \lessapprox 4$. Droplet volume and flow acceleration had marginal influence on depinning threshold for the considered parameter range. Rigorous dimensional analysis, supplemented by statistical examination of the present data and results from previous studies, is employed to identify dominant dimensional groups governing $\mathrm{We}_{h,\mathrm{crit}}$. A new dimensionless group that encapsulates interrelated parameters connected to droplet shape and substrate wettability is proposed, producing good collapse of available data and allowing for a simplified empirical estimation of critical depinning velocity.

DOI: 10.1103/PhysRevFluids.9.034004

I. INTRODUCTION

Droplets under the action of shear flow arise in a large number of engineering applications, such as aircraft and wind turbine icing [1–6], PEM fuel cells [7–10], heat exchangers [11], oil recovery [12,13], and surface cleaning and drying processes [4,14–16]. Driven by widespread engineering applications, droplet depinning under wind-forcing has been the subject of numerous scientific studies (see, e.g., Refs. [6,17–20]). Droplet geometry at depinning can be influenced by its volume [19,20], surface wettability [5,19,21], and surface roughness [22]. Physical properties of the working fluids are affected by ambient temperature and humidity, which are of particular interest for droplets under icing conditions [21]. Drag coefficients of the droplets are also influenced by the incoming flow conditions, such as turbulence intensity [1,15], Reynolds number [23–25], and relative submergence of the droplet in the wall-bounded flows [1].

Milne and Amirfazli [19] investigated the fundamental parameters governing the onset of droplet motion under laminar boundary layer flows. Water and hexadecane droplets with heights in the range of 0.9 to 2.5 times the boundary layer thickness on polymethyl methacrylate (PMMA), Teflon®, and superhydrophobic surfaces (SHS) were tested. They found that wettability of the liquid-solid system was the dominant parameter influencing droplet depinning. An exponential relation $U_{\mathrm{crit}} = ae^{b(L_{b_0}/A_0)^{1/2}}$ was proposed between the critical air velocity required for droplet motion onset, U_{crit}, and the ratio of droplet contact length to side-view area in the sessile state, L_{b_0}/A_0. With this scaling, the results for tests using water droplets collapsed to a self-similar curve. Reasonable agreements were also found for other droplet-substrate systems.

White and Schmucker [20] investigated droplets under combined gravity and wind forcing in a small tiltable wind tunnel. Water droplets of volumes ranging from 15 to 450 μL on a roughened aluminum surface inclined at 0°, 10°, 20°, and 30° were tested. Droplets under pure wind forcing were found to depin at a constant critical Weber number of $\mathrm{We}_{\mathrm{crit}} = \rho U_{\mathrm{crit}}^2 h/\gamma = 7.9$, where ρ is the fluid density, h is the droplet height, and γ is surface tension. They found critical Weber number to decrease with increasing surface inclination angle. The contact line at droplet depinning was observed to be formed by two semicircular arcs at the receding and advancing droplet segments connected by straight line segments aligned with the streamwise direction.

While many existing studies have explored droplet behavior in a laminar boundary layer, little consideration has been given to accelerating turbulent boundary layers on a flat plate. White and Schmucker [1] considered water droplets of volumes ranging from 5 to 150 μL on an aluminum surface in an accelerating turbulent boundary layer. A relatively constant critical Weber number of $\mathrm{We}_{\mathrm{crit}} = 3.45 \pm 0.09$ was found, which is notably lower than that found for laminar boundary layers [20]. Significant unsteadiness observed in the droplet surface prior to depinning was attributed to flow separation and the ensuing unsteady flow in the droplet wake [1]. However, a later study by Milne *et al.* [26] suggests that the frequency of droplet oscillations associate more with the resonance frequency of the droplet-substrate system, which depends on droplet volume, surface tension, and wetting properties, than the frequency of external forcing.

A few recent studies have examined droplet motion on a solid surface in a fully developed turbulent channel flow. Barwari *et al.* [27] investigated the depinning criteria for droplets of pure water and solutions of glycerine and ethanol with varied mass fractions on substrates of PMMA and coated silicon wafer (cSW). The critical droplet Reynolds number, defined as $\mathrm{Re}_{\mathrm{droplet}} = \rho_L h_0 U_{\mathrm{crit}}/\mu_L$, where ρ_L is droplet density, μ_L is droplet viscosity, and h_0 is the initial height of the droplet, plotted against a modified Laplace number defined based on initial droplet streamwise length, L_{b_0}, and wetting parameters, $\mathrm{La} = \rho_L \gamma L_{b_0}/\mu_L^2$, was found to collapse the data from all liquid-substrate systems to a single power-law curve. By approximating droplet geometries as spherical caps, this power-law function yields an empirical model predicting critical depinning velocity based on droplet volume and contact angle in the sessile state. However, when casting the reported critical velocities for pure water droplets into Weber numbers, as proposed by White and Schmucker [1], droplets of volumes ranging from 7.8 to 39.9 μL exhibit Weber numbers in the range $8.2 \lessapprox \mathrm{We}_{\mathrm{crit}} \lessapprox 11.8$ and $8.5 \lessapprox \mathrm{We}_{\mathrm{crit}} \lessapprox 9.1$ on PMMA and cSW surfaces, respectively. Both ranges are significantly higher than $\mathrm{We}_{\mathrm{crit}} \approx 3.45$ for droplets on aluminum surfaces subjected to a zero-pressure-gradient turbulent boundary layer. Unfortunately, detailed flow characterization was not presented in Barwari *et al.* [27]. Whether and how factors such as wetting properties, near-wall flow structure, and turbulence intensity contribute to the discrepancies in critical Weber number remain open questions.

Much attention in prior studies has been focused on finding the critical flow conditions for depinning of an isolated droplet submerged in a flat plate boundary layer. Attempts have also been made to develop a universal model to predict depinning velocities for varying droplet-flow-substrate systems, for example, the empirical relationships proposed by Milne and Amirfazli [19] and Roisman *et al.* [21]. However, comparing test results of these two studies for the same combination of droplet-flow-substrate systems and similar droplet volumes reveals discrepancies in both critical velocities and droplet geometries at depinning. The source of these discrepancies may lie in the effects of the near-wall velocity profile and relative submergence of the droplet in the boundary layer, which are not taken into consideration by most studies but can significantly affect the fluid loading experienced by the droplet [1]. Furthermore, to the authors' knowledge, the influence of the flow acceleration leading to the critical depinning velocity has not been considered. Most studies used quasisteady flow conditions by "slowly" increasing the velocity, while others assumed negligible flow ramp-up time using flow generated by a high-pressure gradient along a flow duct. It is unclear, however, how flow acceleration may affect droplet depinning conditions, if at all. Finally, as opposed to droplet behavior previously considered in flat plate boundary layers, limited attention has been given to droplet removal by impinging jets despite its close relevance to practical

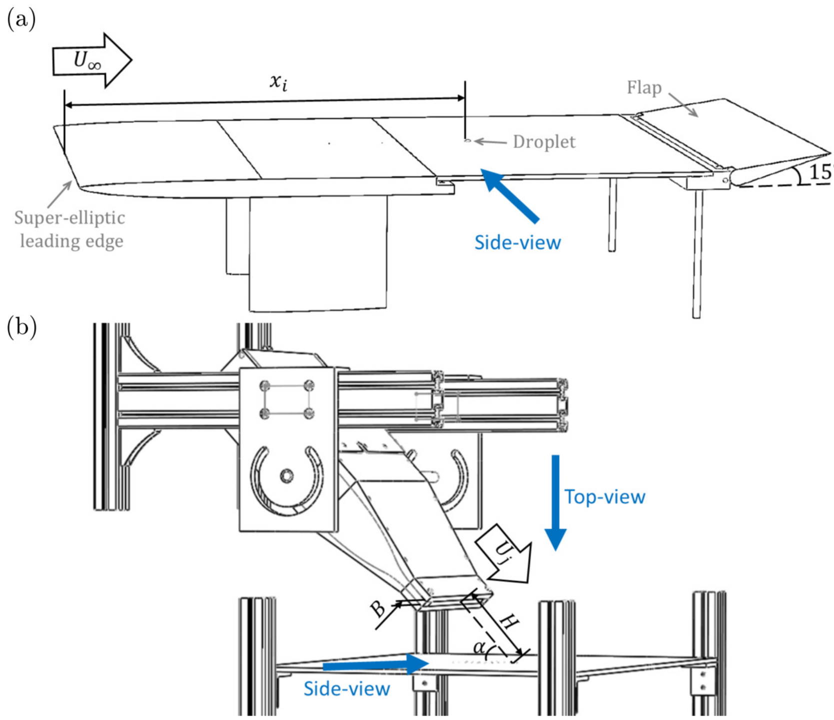

FIG. 1. Experimental setup for droplet depinning under the impact of wall-bounded shear flows formed by (a) flat plate boundary layer and (b) impinging jet.

engineering applications. To the best of the authors' knowledge, there is only one study reporting the jet exit velocity required for surface droplet removal. Leung *et al.* [16] investigated jet velocity requirements for removing distributed millimeter-sized droplets with an impinging round jet. The critical condition was defined as the jet exit velocity at which approximately 50% of the scattered droplets were displaced. Although this study might be informative for a specific jet configuration, it did not detail the flow fields, surface wetting parameters, and droplet behaviors under varied jet configurations.

The aim of the present investigation is to explore the physics of droplet depinning from a horizontal plate under the action of wind forcing in a laminar boundary layer as well as an impinging jet at various impingement angles. The effect of flow acceleration is also examined. Systematic dimensional analysis is employed to clarify the physics and collapse data from the present study and previous literature.

The remainder of the paper is organized as follows: Section II presents details of the experiments, Sec. III discusses data extraction from recorded droplet images, Sec. IV presents results on droplet depinning, Sec. V discusses dimensional analysis and introduces an empirical relation to predict critical depinning velocity, and Sec. VI presents salient conclusions.

II. EXPERIMENTAL SETUP

Droplet behavior subjected to wall-bounded shear flows was investigated using two flow configurations: a zero-pressure-gradient laminar boundary layer formed by flow over a flat plate [Fig. 1(a)], and a wall jet formed by slot jet impingement on a flat plate [Fig. 1(b)]. Exemplary droplet images are shown in Fig. 2. A Cartesian coordinate system is defined with origin at the upstream edge of the droplet in the sessile configuration, with the x coordinate pointing downstream and y oriented in the

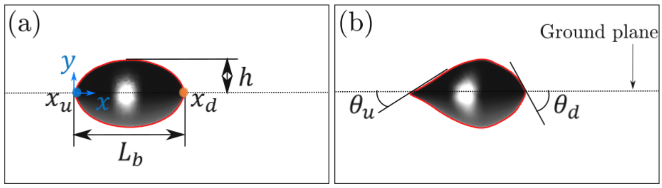

FIG. 2. Side-view geometry of a 120 μL droplet (a) in the sessile state, and (b) prior to depinning, with geometric parameters annotated in the images. Note that the droplet image is reflected about the ground plane.

wall normal direction. The position of the upstream (receding) and downstream (advancing) extent of the droplet are denoted x_u and x_d, respectively. The maximum droplet height (h), streamwise contact length (L_b), and upstream (receding) and downstream (advancing) contact angles (θ_u and θ_d, respectively) are also labeled.

Laminar boundary layer experiments were conducted in the closed-loop wind tunnel in the Fluid Mechanics Research Laboratory at the University of Waterloo, which has a 0.6×0.6 m^2 test section and free stream turbulence intensity of less than 0.06 %. The assembly used to produce laminar boundary layer flow is depicted in Fig. 1(a). A 0.9-m-long flat plate insert spanning the test section was employed as the test surface. Upstream a leading edge component with superelliptic profile [28] was used to minimize flow disturbances due to curvature discontinuities. A trailing edge flap placed downstream of the test plate was set at 15° with respect to the x axis to ensure that the stagnation point was stable and on the lower side of the plate superelliptic leading edge. The virtual origin of the laminar boundary layer was estimated to be located 100 mm upstream of the flat plate leading edge. The thickness of the boundary layer at the droplet location is denoted as δ and the displacement thickness as δ^*.

Impinging jet experiments were performed using a custom jet facility at the University of Waterloo, see Fig. 1(b). A detailed description of flow conditioning prior to the jet nozzle exit can be found in Zhang *et al.* [29]. The conditioned flow exited from a rectangular nozzle of span $L = 200$ mm and height $B = 10$ mm. At the nozzle exit, the velocity profile was nearly uniform, with maximum deviation of less than $\pm1\%$ across 95% of the span. Four jet orientation angles of $\alpha = 30^\circ, 45^\circ, 60^\circ$, and 90° with respect to the horizontal test plate (the x axis) were considered at a fixed nozzle-to-plate spacing ratio of $H/B = 4$, see Fig. 1(b).

The test surface for both flow facilities was an anodized aluminum plate polished with 1000-grit sandpaper, resulting in an estimated surface roughness 0.10 ± 0.05 μm. Droplets of distilled water of volumes 75, 90, 105, and 120 μL were placed on the test plate using a micropipette (Scilogex) at a distance x_i from (a) the flat plate leading edge for the laminar boundary layer studies and (b) the intersection point of the jet centerline and the target surface for the impinging jet experiments. An additional parameter x^* is defined as the streamwise distance from the virtual origin of the flat plate model or the stagnation point of the impinging jet at a given jet configuration, which is characterized in detail by Zhang *et al.* [29]. Uncertainty in droplet volume is estimated to be less than 2.3 μL as quantified based on weight measurement using an analytical balance. Droplet placement followed the procedure of de Gennes [30], such that the sessile droplets had initial contact angle θ_0, matching the advancing contact angle for the substrate-fluid combination.

In both flow facilities, the incoming flow velocity was increased from 0 to 20 m/s via nearly linear accelerations of $\mathrm{d}U_\infty/\mathrm{d}t$ (or $\mathrm{d}U_j/\mathrm{d}t$ for the jet facility) $=$1.2, 2.2, and 4.4 m/s^2. The incoming flow velocities were characterized using a normal hot-wire probe (Dantec 55P11) connected to a constant-temperature anemometer (Dantec Streamline Pro). The probe was calibrated *in situ* against a Pitot-static tube, with an estimated uncertainty in free stream measurements of less than 0.3%. Hot wire signals were sampled at 10 kHz and low-pass filtered at 5 kHz. The hot-wire position relative to the plate was measured via calibrated side-view camera images. Uncertainty in the hot-wire position was estimated to be approximately 88 μm. In the wind tunnel, instantaneous velocities were

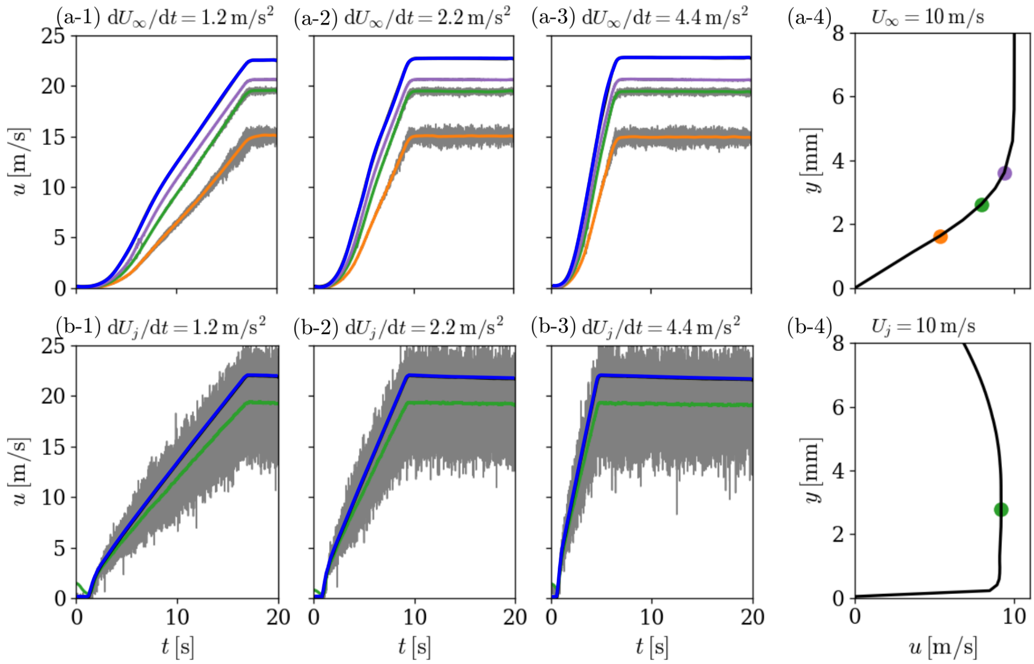

FIG. 3. Sliding average of velocity sampled in the freestream or at the jet exit (blue lines) and three near-wall locations as the flow speed ramps up at 1.2 m/s^2 (column 1), 2.2 m/s^2 (column 2), and 4.4 m/s^2 (column 3), overlaid with instantaneous velocities measured over five runs (gray lines). Steady near-wall velocity profile (column 4) measured at a free stream velocity or jet exit velocity of $U = 10$ m/s, with dots showing the wall-normal locations where the near-wall velocity ramp-up time histories are sampled. Near-wall velocity profiles and ramp-up time histories measured at $x_i = 550$ mm downstream of the flat plate leading edge (row 1), and at $x^* = 20$ mm downstream of the stagnation point of impinging jets oriented at $\alpha = 45^\circ$ (row 2) are shown as examples.

sampled using hot-wire anemometry within the free stream along the centerline of the recirculating wind tunnel (at $y \approx 150$ mm), and at three near-wall locations close to the mean droplet height ($y \approx 2.6$ mm) at $x_i \approx 550$ mm. For the impinging jet facility, instantaneous velocities were sampled along the jet centerline at the jet exit, and at several streamwise locations corresponding to droplet deposition locations used for the full study.

The velocity time histories corresponding to the three investigated accelerations are shown in Fig. 3 (columns 1–3), along with the approximate measurement locations with respect to the local boundary layer velocity profile (column 4). Measurements were repeated for five trials at each wall-normal location for each acceleration. The instantaneous velocities measured by hot-wire are indicated by the gray lines. A moving average of the velocity measurements of each trial was calculated using a second-order Savitzky-Golay filter [31] with a window width of five seconds. In the wind tunnel at the sampling location closest to the wall (Fig. 3, row 1, orange lines), the local flow acceleration (slope of the line) and the final velocity are notably smaller than those in the freestream (Fig. 3, row 1, blue lines) for all flow accelerations. This is expected given the velocity gradient in the steady velocity profile in the near-wall region [Fig. 3(a-4)]. Velocity fluctuations around the moving average are the highest for this measurement location. Near the droplet height (Fig. 3, row 1, green lines), the slope is similar to that of the free stream, and the velocity fluctuations quickly diminish. Further away from the flat plate surface (Fig. 3, row 1, purple lines), both slope and final velocity approach those of the free stream. Velocity fluctuations at this location are negligibly small, similar to the amplitude of those in the free stream.

TABLE I. Test parameters. Incoming flow conditions and boundary layer parameters are characterized at $U_\infty = U_j = 10$ m/s.

α [deg]	x_i [mm]	x^* [mm]	δ [mm]	δ^* [mm]	$\forall$ [μL]	dU/dt [m/s^2]	θ_0 [deg]
0	550	650	4.7	1.6			86.1 ± 2.7
45	10	20	2.6	0.21			81.0 ± 1.5
45	30	40	2.2	0.34	75, 90,		80.8 ± 2.1
						1.2, 2.2, 4.4	
45	40	50	3.1	0.40	105, 120		80.5 ± 1.4
45	60	70	4.2	0.47			85.9 ± 1.3
90	70	70	3.2	0.28			81.8 ± 2.0
30	39	60	3.4	0.45			84.4 ± 1.9
					75, 120	1.2, 2.2, 4.4	
60	45.5	50	3.5	0.42			78.2 ± 2.1

For the impinging jet facility, while velocity fluctuations at the jet exit are negligibly small (Fig. 3, row 2, blue lines), the velocity fluctuations around the moving average (Fig. 3, row 2, green lines) are significantly higher than that in the laminar boundary layer. This is mainly attributed to the impingement of large-scale vortical structures formed in the free jet region [29]. Note that only a single measurement point above the flat plate was tested in this facility owing to the marginal difference in velocity with y around the droplet height. In both the wind tunnel and the jet facility, the instantaneous and moving-averaged velocity time traces of the five trials of each combination of acceleration, streamwise location, and wall-normal location show high repeatability.

Table I summarizes the test parameters. Preliminary measurements suggested most droplet depinning occurs at a free stream (or jet exit) velocity of around 10 m/s, and thus the boundary layer thickness at this velocity at the position of sessile droplet placement was used to estimate the relative submergence of the droplet, δ/h_0. Fourteen runs were performed for each combination of parameters listed in Table I.

A CMOS camera (pco.edge 5.5) operating at 40 Hz was used to capture side-view images of the droplets. The camera was equipped with a 200 mm Nikon lens to capture a field-of-view (FOV) of 45×20 mm^2 with a cropped sensor size of 2560×1162 px. This resulted in a magnification factor of $M = 0.199$ and spatial resolution of 17.6 μm/px. Cold diffused light provided by an LED light array (Amaran H528) was used as backlight to improve image contrast. A Nikon D7200 camera equipped with a 50 mm Nikon lens operating at 1 Hz was used to provide additional top-view images [see Fig. 1(b)]. Triggering signals for the free stream velocity control and the side-view and top-view cameras were synchronized using a custom LabVIEW virtual instrument (National Instruments).

III. DROPLET IMAGE POSTPROCESSING

Subpixel polynomial fitting (SPPF) [32] was used to quantify geometric parameters from the raw droplet images. Briefly, SPPF first detects the droplet boundary with pixel resolution using Canny edge detection with Otsu's threshold [33]; the droplet boundary is separated from the Canny edge map using a marching squares contour-finding algorithm [32]. Then, sigmoid functions [34] are fitted to the pixel intensity around each pixel on the detected boundary and the locations of the refined droplet edge with subpixel resolution are found at the saddle points of the sigmoid.

Locations of the contact points were found at the intersections between the droplet edge with its reflection [see Fig. 2(a)]. Contact angles were calculated from the local slope of a fitted second-order polynomial around the contact points; the optimum number of pixels used in curve fitting was found by systematically increasing the number of pixels until variation in calculated contact angles

TABLE II. Initial droplet geometries.

$\forall$ [μL]	L_{b_0} [mm]	h_0 [mm]	θ_0 [deg]
75	7.7 ± 0.1	2.5 ± 0.1	82.0 ± 2.5
90	8.3 ± 0.2	2.6 ± 0.1	81.2 ± 3.2
105	8.7 ± 0.2	2.7 ± 0.1	83.0 ± 2.9
120	9.1 ± 0.2	2.8 ± 0.1	83.5 ± 3.4

was less than 0.1°. For contact angles in the range of $10^\circ \leqslant \theta_c \leqslant 160^\circ$, as in the present study, the uncertainty associated with contact angle measurement using SPPF is within 1° [32]. Table II summarizes the sessile state statistics of the investigated droplets and suggests good consistency in droplet initial length L_{b_0}, initial height h_0, and initial contact angle θ_0. Variability in sessile contact angle estimates of a given droplet volume are within 3.5°, indicating good repeatability in the droplet placement process.

IV. CRITICAL DROPLET DEPINNING CONDITIONS

In this section we select a 120 μL droplet placed at $x^* = 70$ mm downstream of the stagnation point in the jet facility with $\alpha = 45^\circ$ and $dU_j/dt = 4.4$ m/s as an example to highlight features of droplet depinning. Figure 4 shows the typical response of a droplet [Figs. 4(b-1) to 4(b-6)] under

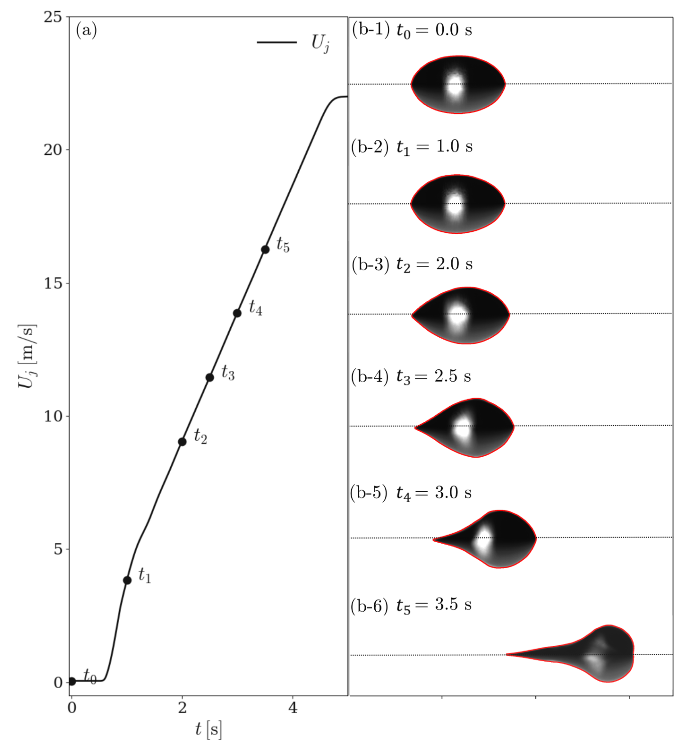

FIG. 4. Example of a 120 μL droplet subjected to a shear flow generated by an accelerating impinging jet with $\alpha = 45^\circ$ and $dU_j/dt = 4.4$ m/s^2. The droplet is placed at $x^* = 70$ mm downstream of the jet stagnation point. (a) Velocity ramp-up profile at jet exit. (b-1)–(b-6) Typical droplet deformation and runback at various time points indicated in panel (a).

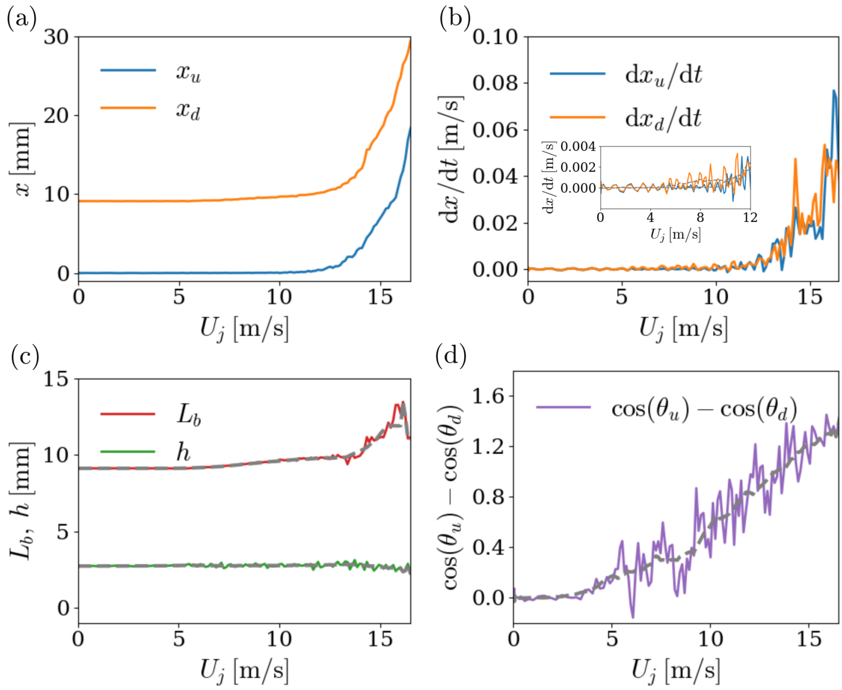

FIG. 5. Typical (a) displacement and (b) velocity of droplet contact points (blue and orange lines: upstream and downstream contact points, respectively; inset: zoom-in view of contact point velocity in the jet exit velocity range of $U_j \leqslant 12$ m/s), (c) droplet contact length (red line) and height (green line), and (d) contact angle hysteresis (purple line) with increasing jet exit velocity of a 120 μL droplet under the impact of shear flow formed at $x^* = 70$ mm downstream of the stagnation point of a $\alpha = 45^\circ$ accelerating impinging jet at $\mathrm{d}U_j/\mathrm{d}t = 4.4$ m/s^2 is shown as exemplar. Trend lines (gray dashed lines) are acquired by computing the moving average with a window size corresponding to $\Delta t = 0.25$ s.

the influence of an accelerating shear flow [Fig. 4(a)]. As the incoming flow velocity increases from zero, the droplet deforms due to aerodynamic loading (t_0 to t_2), continually attaining a new shape for which the external loading is balanced by increased adhesion, characterized by an increase in contact angle hysteresis, CAH $= [\cos(\theta_u) - \cos(\theta_d)]$. When aerodynamic loading from the shear flow exceeds adhesion forces, the droplet depins from the initial location t_2 and sheds along the surface (t_3 to t_5).

Figure 5 presents quantitative data extracted from side-view images of the case presented in Fig. 4. Figure 5(a) shows the change of droplet contact point position with jet exit velocity. The velocities of the contact points are shown in Fig. 5(b). The velocity of the center of mass of the droplet can be roughly approximated as the average of the advancing and receding contact point velocities. Droplet height and contact length are presented in Fig. 5(c), and contact angle hysteresis is shown in Fig. 5(d). Trend lines of contact point velocities, droplet height, contact length, and contact angle hysteresis versus instantaneous jet exit velocity are acquired by computing a moving average with window size corresponding to $\Delta t = 0.25$ s for statistical analysis.

Berejnov and Thorne [35] identified three transitional events exhibited by a droplet under increasing external forcing: (i) depinning of the downstream portion of the contact line; (ii) depinning of the upstream portion of the contact line; and (iii) depinning of the entire contact line which gives rise to translational motion of the droplet along the surface. For jet velocities $0 \lessapprox U_j \lessapprox 5$ m/s, both contact points remain pinned [Fig. 5(a)], although contact angle hysteresis increases [Fig. 5(d)], signaling deformation of the droplet in response to increased aerodynamic loading. The contact point velocities [Fig. 5(b)] are zero in this range, with slight undulations observed due to uncertainty in the contact point positions, and the droplet length and height [Fig. 5(c)] remain unchanged.

As the jet velocity increases to $5 \lessapprox U_j \lessapprox 9$ m/s, the first transitional event occurs, wherein the downstream (advancing) contact point first depins, while the upstream contact point remains fixed, see the inset in Fig. 5(b). This leads to an increase in contact length, although droplet height remains largely unchanged [Fig. 5(c)]. Contact angle hysteresis continues to increase, on average, with large fluctuations observed [Fig. 5(d)] due to oscillations of the air-water interface [27,36].

At still higher jet velocities of $9 \lessapprox U_j \lessapprox 12$ m/s the upstream (receding) contact point depins, corresponding to the second transitional event. Although difficult to discern from the quantitative data, during this phase the droplet tends to saltate along the surface, intermittently depinning and stopping, as reported in previous studies [6,37] [see the "stair step" motion of the contact points in Fig. 5(a) and increasing amplitude of the contact point velocity fluctuations in Fig. 5(b) inset]. Droplet contact length continues to increase in this velocity range with little change in height [Fig. 5(c)]. Still further increases in jet speed results in both contact points completely depinning and the droplet accelerating as it moves along the surface [Fig. 5(b)], corresponding to the third transitional event. Here, elongation in droplet contact length is more significant than in the first two transitional events. It is accompanied by a slight decrease in droplet height [Fig. 5(c)] and diminished fluctuations, albeit with continued increase, on average, of contact angle hysteresis [Fig. 5(d)].

Droplet depinning is herein defined as the time instant when the pixel displacement of the upstream contact point exceeds a set threshold of 6–8 pixels, depending on the case (see Ref. [38] for details on threshold selection). Critical depinning velocities expressed in terms of the freestream $U_{\infty,\text{crit}}$ (for boundary layer configuration) or jet exit velocity $U_{j,\text{crit}}$ (for impinging jet configuration) and incoming shear layer velocity at the droplet height $U_{h,\text{crit}}$ (for both configurations) are presented in Fig. 6 for all cases considered. Error bars represent standard deviation over the fourteen trials for each case. A slight, albeit statistically significant, decreasing trend with droplet volume is observed ($p < 0.05$ from paired t tests [39] between the smallest and largest volumes), which aligns with previously reported trends [19,21]. Similarly, for all flow configurations, critical velocity increases marginally with flow acceleration ($p < 0.05$ from paired t tests between the smallest and largest accelerations).

The effects of incoming flow orientation angle α and relative submergence δ^*/h on critical depinning velocity $U_{h,\text{crit}}$ are presented in Fig. 7, wherein we have averaged data across all considered volumes for a given α, $\mathrm{d}U/\mathrm{d}t$, and x^*. For impinging-jet cases with $30^\circ \leqslant \alpha \leqslant 60^\circ$, the mean depinning velocity is within the range of $8 \lessapprox U_{h,\text{crit}} \lessapprox 10$ m/s, with modest influence of α and x^*. Variations in depinning velocities in these test cases are believed to be caused mainly by spatial heterogeneities of the substrate surface that lead to slightly different sessile contact angles with varying x^* (see Table I), and thus can be considered to be within experimental uncertainty. Significantly higher depinning velocities of around $U_{h,\text{crit}} \approx 13$ m/s are found for droplets submerged in the flat plate boundary layer ($\alpha = 0^\circ$), which is due to the higher relative submergence [$\delta^*/h \approx 0.6$ as compared with $0.1 \lessapprox \delta^*/h \lessapprox 0.2$ for the impinging jet cases, see Fig. 7(b)] and the resulting reduced flow momentum experienced by the droplet. The average flow speed experienced by droplets in the flat plate boundary layer is 4.2 m/s compared with 5.6–7.5 m/s for the impinging jet cases. The droplet shapes during runback are similar across flow conditions, as shown in Fig. 8, implying similar drag coefficient. This suggests that, for the cases considered in the present investigation, the drag force on droplets in the boundary layer is up to a factor of two lower than for droplets in the impinging jet flows, hence requiring higher critical velocity to depin the droplets in the boundary layer.

On the other hand, Fig. 7(a) indicates that considerably lower depinning velocities of around $U_{h,\text{crit}} \approx 7$ m/s are attained in the normal jet impingement cases ($\alpha = 90^\circ$). This is despite the relative submergence [see Fig. 7(b)] and the free stream fluctuating velocity being similar for all impinging jet cases. Despite similarities in submergence and the magnitude of incoming flow fluctuations, droplets subjected to normal jet impingement exhibit more pronounced oscillations

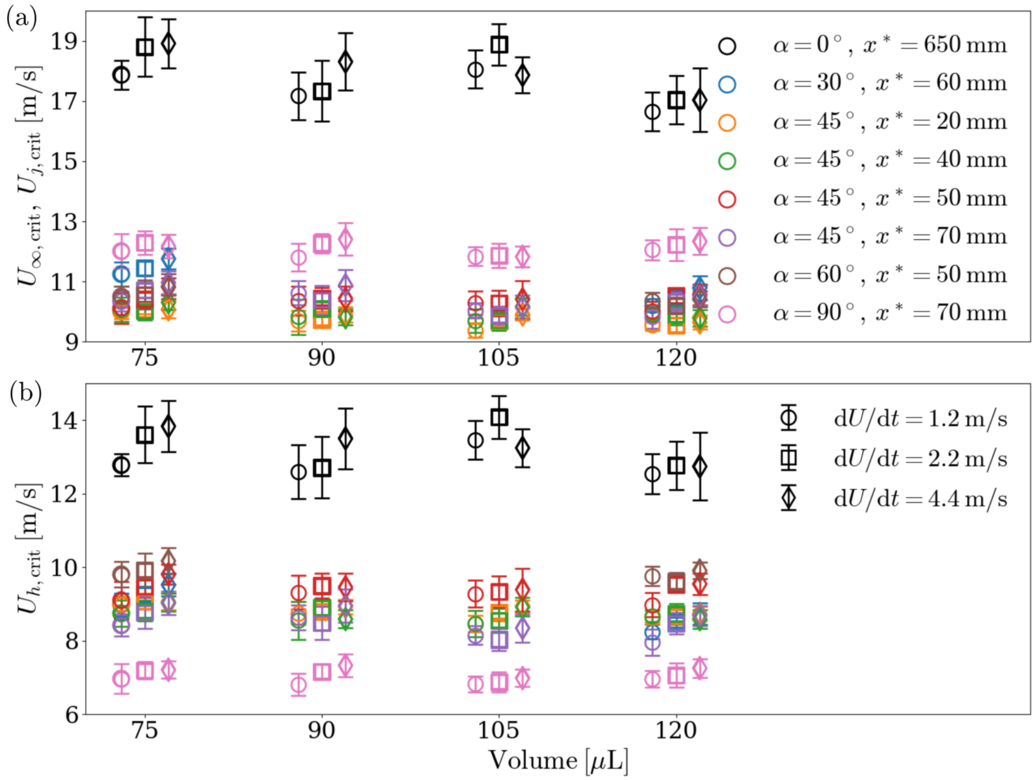

FIG. 6. Critical droplet depinning velocities (a) measured in the freestream, U_∞, or at the jet exit, U_j, and (b) measured at droplet height U_h as a function of droplet volume under background flow configurations listed in Table I.

than those in other impinging jet cases, see Figs. 8(b) and 8(c), which likely elicits earlier depinning due to the dynamic motion.

Figure 9 presents droplet contact length, height, and contact angle hysteresis at depinning for all considered cases. At lower flow acceleration, droplets elongate in the streamwise direction and flatten in height more than at the higher accelerations [see Figs. 9(a) and 9(b)]. The influence of flow acceleration on contact angle hysteresis is more notable, with CAH increasing with flow acceleration [Fig. 9(c)], which correlates with the observed higher critical depinning velocity for larger accelerations (see Fig. 6). Droplet height is not influenced by α, whereas droplet length and CAH tend to decrease slightly with increasing α. There is a more pronounced difference between droplet length and CAH when comparing the flow modalities, with droplets in a boundary layer stretching more and having larger CAH, which indicates increased adhesion. Both factors contribute to the higher critical velocities demonstrated by droplets submerged in a laminar flat plate boundary layer.

V. DIMENSIONAL ANALYSIS OF CRITICAL DEPINNING CONDITIONS

As discussed in Sec. IV, critical velocity $U_{h,\text{crit}}$, droplet height h, contact length L_b, and contact angle hysteresis CAH are primarily influenced by incoming flow orientation angle α and relative submergence δ^*/h (Figs. 6 and 9). In this section we employ dimensional analysis in an effort to tease out the prominent dimensionless variables driving trends observed in the present and previously published data.

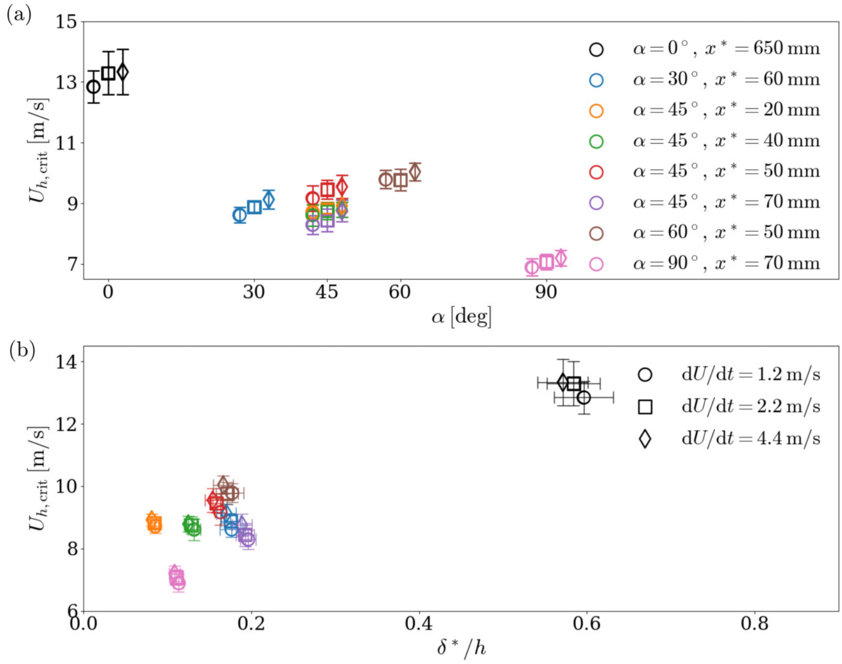

FIG. 7. Critical droplet depinning velocities, $U_{h,\mathrm{crit}}$, averaged across all droplet volumes, as a function of (a) background flow orientation angle α, and (b) relative submergence δ^*/h at depinning.

The depinning process is governed by the force balance between the driving and the resisting forces. For droplets on a horizontal surface, aerodynamically induced drag on the droplet F_D is the sole driving force. This force can be decomposed into pressure drag and skin friction at the air-water interface. The forces resisting the onset of droplet motion are adhesion F_{adh} due to contact angle hysteresis and viscous forces F_μ arising from droplet elongation.

Adhesion can be estimated by $F_{\mathrm{adh}} \propto \gamma L_b(\cos\theta_u - \cos\theta_d)$, with γ being the surface tension of water [19,21,40]. The viscous force F_μ due to a moving contact line can be estimated as $F_\mu \propto \mu_L v_{\mathrm{drop}} L_b^2/h$ [41], where μ_L is the dynamic viscosity of water and v_{drop} is the velocity of the droplet center of mass, which is on the order of the speed of the downstream contact point. Order of magnitude estimation demonstrates that F_μ is four order of magnitudes smaller than F_{adh} and can thus be neglected for the present study. Furthermore, since acceleration of the droplet center

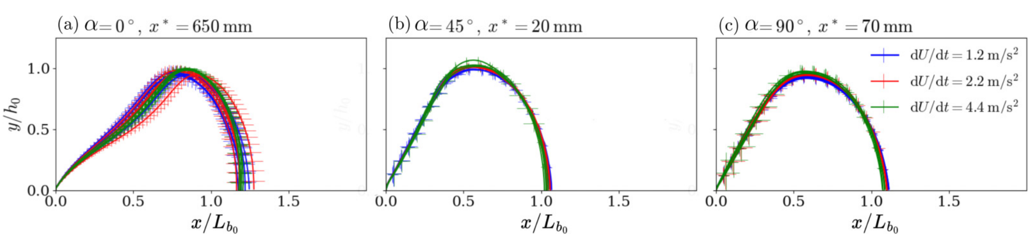

FIG. 8. Mean side-view geometry of droplets prior to depinning under shear flows formed (a) by a flat plate boundary layer, (b) for $\alpha = 45^\circ$ impinging jet with $x^* = 20$ mm, and (c) for $\alpha = 90^\circ$ impinging jet with $x^* = 70$ mm. Lengths in horizontal and vertical directions are normalized by initial droplet contact length and height, respectively.

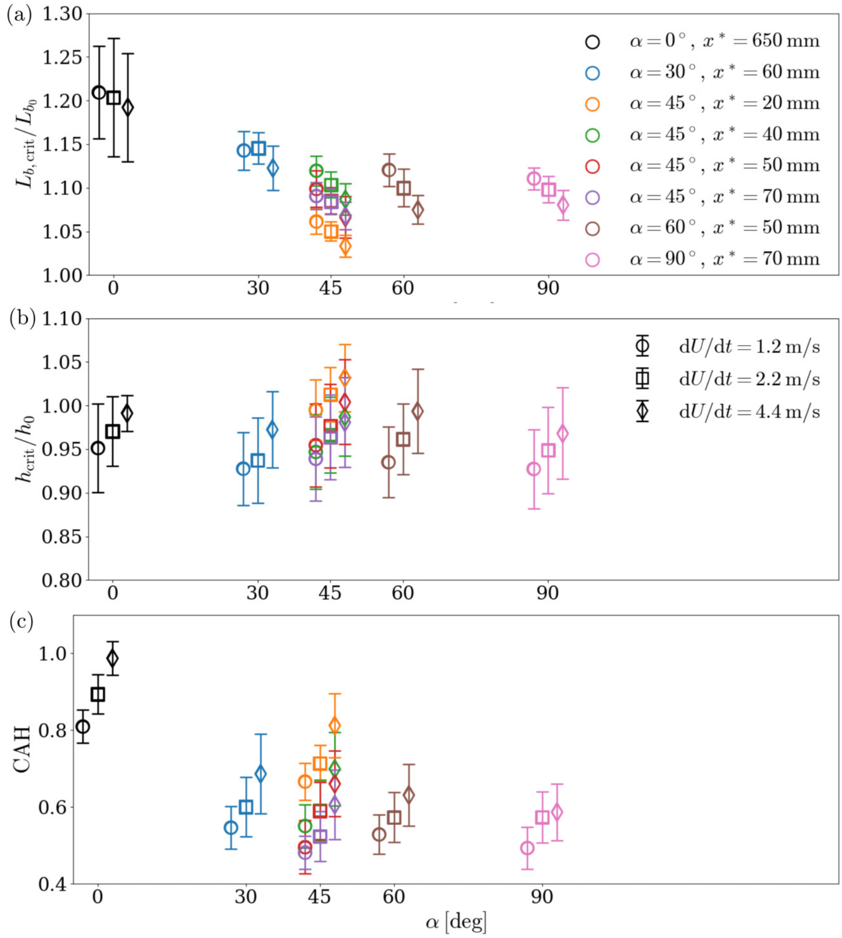

FIG. 9. Droplet (a) contact length, (b) height, and (c) contact angle hysteresis at depinning, averaged across all droplet volumes as a function of background flow orientation angle α.

of mass is relatively small [19], the force balance at droplet depinning reduces to

$$F_D = F_{\mathrm{adh}}. \tag{1}$$

The forces in Eq. (1) are functions of

$$F_D = f_1(\rho, \mu, U_h, \delta^*, h, \psi(l), \theta(l)), \tag{2a}$$

$$F_{\mathrm{adh}} = f_2(\gamma, \psi(l), \theta(l)), \tag{2b}$$

where ρ and μ are air density and dynamic viscosity, respectively, and $\psi(l)$ and $\theta(l)$ are three-dimensional (3D) contact line shape and contact angle distribution along the contact line l, respectively. Contact angle distribution $\theta(l)$ can be crudely approximated from two-dimensional (2D) side-view droplet images by the upstream and downstream contact angles, θ_u and θ_d, respectively, and $\psi(l)$ by contact length L_b. From Eqs. (1) and (2), it can be noted that critical depinning velocity is a function of several variables,

$$U_h = f(\rho, \mu, \gamma, \delta^*, h, L_b, \theta_u, \theta_d), \tag{3}$$

which serves as the foundation of our dimensional analysis.

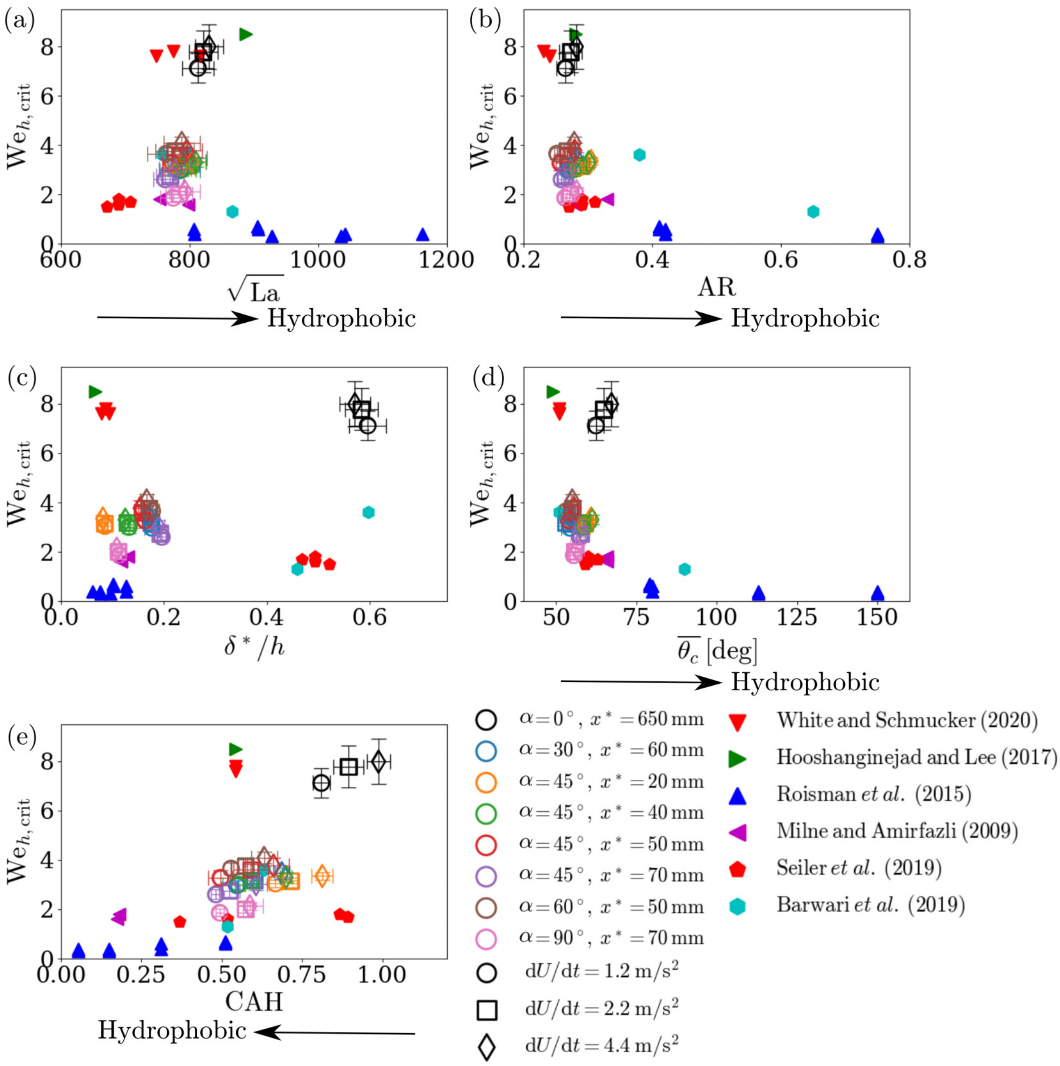

FIG. 10. Critical Weber number $\mathrm{We}_{h,\mathrm{crit}}$ as a function of (a) $\sqrt{\mathrm{La}}$, (b) AR, (c) δ^*/h, (d) $\overline{\theta}_c$, and (e) CAH.

Using ρ, γ, and h as repeating variables, the dimensional relation in Eq. (3) can be recast in dimensionless form as

$$\mathrm{We}_h = \mathcal{F}(\sqrt{\mathrm{La}}, \mathrm{AR}, \delta^*/h, \overline{\theta_c}, \mathrm{CAH}). \tag{4}$$

where $\mathrm{We}_h = \rho U_h^2 h/\gamma$ is the Weber number based on droplet height at depinning, $\mathrm{La} = \rho h \gamma/\mu^2$ is the modified Laplace number, $\mathrm{AR} = h/L_b$ is the aspect ratio of the droplet at depinning, δ^*/h is the relative droplet submergence in the shear flow, and $\overline{\theta_c} = (\theta_u + \theta_d)/2$ is the mean contact angle at depinning.

Critical Weber number is plotted versus the other dimensionless parameters in Eq. (4) in Fig. 10. The results of the present study are complemented by the data obtained for water droplets on substrates of varied wettabilities reported in literature (see Table III). In the present study, under the influence of the laminar flat plate boundary layer droplets depin within a Weber number range of $7 \leqslant \mathrm{We}_h \leqslant 8$, which is comparable to the value of 7.9 reported by White and Schmucker [20]

TABLE III. Critical depinning conditions for water droplets reported in literature; studies marked with ✠ are experiments conducted in turbulent channel flows, whereas all others were conducted in laminar boundary layers formed over flat plates. Droplet geometries reported in the table are partially extracted from digitized plots or estimated based on geometric correlations assuming a sessile droplet to be a spherical cap [41]. Displacement thickness is estimated based on the Blasius solution and Prandtl approximation [42] for laminar boundary layers and turbulent channel flows, respectively.

	Substrate	$\mathcal{V}$ [μL]	$\sqrt{\text{La}}$	AR	$\mathcal{K}$	$\overline{\theta}_c$ [deg]	CAH	δ^*/h	We_h
Milne and Amirfazli [19]	PMMA	58	753	0.33	1.02	66	0.181	0.131	1.8
		100	798	0.28	0.93	66	0.175	0.117	1.6
Roisman *et al.* [21]	PDMS	50	807	0.41	0.92	79	0.510	0.127	0.6
		100	906	0.41	0.92	79	0.510	0.101	0.7
	PMMA	50	808	0.42	0.92	80	0.310	0.127	0.4
		100	907	0.42	0.92	80	0.310	0.101	0.6
	Teflon	50	928	0.75	1.31	113	0.150	0.096	0.3
		100	1042	0.75	1.31	113	0.150	0.076	0.4
	SHS	50	1035	1.88	4.28	150	0.054	0.077	0.3
		100	1162	1.88	4.28	150	0.054	0.061	0.4
Hooshanginejad and Lee [43]	Aluminium (rough)	130	887	0.28	0.61	49	0.543	0.066	8.5
White and Schmucker[20]	Aluminium (rough)	75	748	0.24	0.76	51	0.543	0.093	7.6
		100	775	0.23	0.75	51	0.543	0.087	7.8
		125	816	0.24	0.76	51	0.543	0.078	7.6
Seiler *et al.* [41]✠	Aluminium	35	707	0.31	0.82	63	0.891	0.469	1.7
	Aluminium (varnished)	35	689	0.29	0.81	60	0.517	0.494	1.6
	PMMA	35	671	0.27	0.85	59	0.369	0.521	1.5
	Steel (varnished)	35	689	0.29	0.83	60	0.866	0.494	1.8
Barwari *et al.* [27]✠	PMMA	39.9	758	0.38	0.92	51	0.632	0.598	3.6
	Silicon (coated)	39.9	866	0.65	1.20	90	0.518	0.459	1.3

for water droplets on aluminum surface submerged in a comparable incoming flow. For droplets in impinging jets, however, notably lower values in the range $2 \leqslant \text{We}_h \leqslant 4$ are observed.

Figures 10(a) and 10(b) show We_h versus $\sqrt{\text{La}}$ and AR at droplet depinning, respectively. Despite the notable difference in side-view geometry observed in the flat plate boundary layer and impinging jets (see Fig. 8), droplets under all the flow configurations considered in the present study fall within fairly tight ranges for these two parameters ($750 \leqslant \sqrt{\text{La}} \leqslant 850$ and $0.25 \leqslant \text{AR} \leqslant 0.30$). By comparison with the data reported in literature, it can be inferred that these two parameters are predominantly influenced by substrate wettability, i.e., an increase in substrate hydrophobicity leads to an increase in $\sqrt{\text{La}}$ and AR.

Droplets in the present study subjected to impinging jets exhibit an increasing trend of We_h with δ^*/h [see Fig. 10(c)], which is expected since greater submergence results in lower effective velocity, and thus lower aerodynamic drag, experienced by the droplet. Similar trends are seen in data from Milne and Amirfazli [19] (purple triangles), Roisman *et al.* [21] (blue triangles), and Barwari *et al.* [27] (cyan hexagons). However, data from different studies do not follow the same trend line, which is due to the variation in other parameters. Comparing $\text{We}_{h,\text{crit}}$ in the laminar boundary layer of the present study (black markers) to those in turbulent channel flows reported by Seiler *et al.* [41] (red pentagons) and Barwari *et al.* [27] (cyan hexagons), droplets depin at lower critical Weber numbers in turbulent channel flows than in laminar boundary layer of similar δ^*/h. The reduced critical Weber number in turbulent channel flows is due primarily to a higher effective

TABLE IV. Linear correlations between the dimensionless parameters on the right-hand side of Eq. (4) measured using the Pearson correlation coefficient [39]. Red, orange, blue, and green indicate very strong, strong, moderate, and weak correlations, respectively.

	$\sqrt{\mathrm{La}}$	AR	δ^*/h	$\overline{\theta}_c$	CAH
$\sqrt{\mathrm{La}}$	1	0.88	−0.18	0.91	−0.58
AR		1	−0.22	0.94	−0.64
δ^*/h			1	−0.16	0.56
$\overline{\theta}_c$				1	−0.69
CAH					1

velocity averaged over the droplet height, which results from a fuller near-wall velocity profile as compared with laminar boundary layers of comparable δ^*.

Figures 10(d) and 10(e) show the dependence of We_h on mean contact angle $\overline{\theta_c}$ and contact angle hysteresis CAH, respectively. Droplets submerged in a laminar boundary layer and impinging jets of the present study exhibit similar mean contact angles of around 80°. Contact angle hysteresis of droplets in impinging jets clusters around CAH ≈ 0.6, while higher values around CAH ≈ 0.9 are exhibited by droplets submerged in the flat plate boundary layer. A comparative analysis with data reported in the literature suggests that increasing substrate hydrophobicity leads to an expected increase in $\overline{\theta_c}$ and decrease in CAH. The latter leads to decreased adhesion between droplet and substrate, and consequently results in lower $\mathrm{We}_{h,\mathrm{crit}}$.

Identifying independent primitive variables in Eq. (3) should lead to independent dimensionless variables in Eq. (4). However, the observed variations of $\mathrm{We}_{h,\mathrm{crit}}$ with $\sqrt{\mathrm{La}}$, AR, and $\overline{\theta_c}$ in Fig. 10 suggest potential dependence between these dimensionless groups. This is assessed using the Pearson correlation coefficient ϱ_P [39], with results summarized in Table IV. Very strong ($\varrho_P \geqslant 0.80$) linear correlations are found by each combination of $\sqrt{\mathrm{La}}$, AR, and $\overline{\theta}_c$, and there is strong correlation ($\varrho_P \geqslant 0.60$) between CAH and both AR and $\overline{\theta}_c$, which in aggregate indicate that the effect of surface wettability is encoded in droplet geometry at depinning. Positive correlation between δ^*/h and CAH reflect the earlier observation that droplets in the laminar flat plate boundary layer of higher submergence attain higher contact angle hysteresis at depinning than those in the impinging jets of lower submergence.

Given the correlation between dimensionless groups, we seek an alternative independent dimensionless parameter. Noting that CAH, $\overline{\theta}_c$, and AR relate to droplet shape, which is in turn related to surface wettability, we aim to condense these parameters. Specifically, a volumetric shape factor $\mathcal{K} = \mathcal{V}/(\pi h L_b^2/6)$ is proposed, which encodes the deformation of a droplet at depinning by comparing its volume to that of a semi-ellipsoid with height h and base diameter L_b. This encapsulates substrate wettability as well since increasing substrate hydrophobicity will decrease contact length (and increase height) and result in an increase in $\mathcal{K}$. While this grouping is chosen based on its utility for a priori prediction of depinning velocity of a given sessile droplet, other groupings of the identified interdependent geometric parameters can be explored.

To assess the strength of the dependence of $\mathrm{We}_{h,\mathrm{crit}}$ on the remaining set of dimensionless parameters, $\sqrt{\mathrm{La}}$, δ^*/h, and $\mathcal{K}$, we compute Spearman's rank correlation coefficients (ϱ_S) [39]. Table V presents the obtained coefficients, confirming that $\mathrm{We}_{h,\mathrm{crit}}$ is strongly related to $\mathcal{K}$, but correlations with $\sqrt{\mathrm{La}}$ and δ^*/h are much weaker. This indicates for a given combination of working fluids (i.e., air and water in the present study), the critical Weber number at depinning is dominated by the dimensionless group associated with depinning geometries.

In light of Table V, we plot $\mathrm{We}_{h,\mathrm{crit}}$ versus $\mathcal{K}$ in Fig. 11. Data for droplets in impinging jets for the present study have $0.80 \leqslant \mathcal{K} \leqslant 0.90$, while droplets in the laminar boundary layer of the present study have $\mathcal{K} \approx 0.65$. When compared with depinning conditions reported for droplets on substrates of varied wettabilities in previous investigations, droplets in impinging jets from our study

TABLE V. Spearman's rank correlation coefficients [39] showing the strength of dependence of $\mathrm{We}_{h,\mathrm{crit}}$ on the remaining dimensionless variables. Red, orange, blue, and green indicate very strong, strong, moderate, and weak correlations, respectively.

	$\sqrt{\mathrm{La}}$	δ^*/h	$\mathcal{K}$
$\mathrm{We}_{h,\mathrm{crit}}$	−0.23	0.30	−0.88

exhibit geometric characteristics similar to those submerged in boundary layer flows over a more hydrophobic surface. We note that, enticing as the prospect may be, computing $\mathcal{K}$ based upon initial (sessile) conditions does not result in the data collapsing as well as in Fig. 11.

The experimental results of the present study and the data reported by other researchers collapse well using $\mathcal{K}$ as the sole control parameter. Fitting a power-law profile to the data in Fig. 11 of the form $\mathrm{We}_{h,\mathrm{crit}} \approx a\mathcal{K}^{-\beta}$ yields fitting coefficients of $a = 1.5 \pm 0.17$ and $\beta = 4.0 \pm 0.34$. Using the nominal values of a and β, the equation of best fit can be rearranged to produce the following empirical relation for critical depinning velocity

$$U_{h,\mathrm{crit}} \approx 0.336\frac{\gamma^{1/2}h^{3/2}L_b^4}{\rho^{1/2}2}. \tag{5}$$

Equation (5) provides an approach for estimating critical depinning velocity that depends only on data that are relatively easy to obtain experimentally. Unlike the computationally demanding subpixel resolution required to measure contact angles with high accuracy, the droplet contour yielded by Canny edge detection is sufficient for good measures of droplet height h and contact length L_b. In addition, as can be observed in Figs. 4(b-3) to 4(b-5), droplet height and contact length

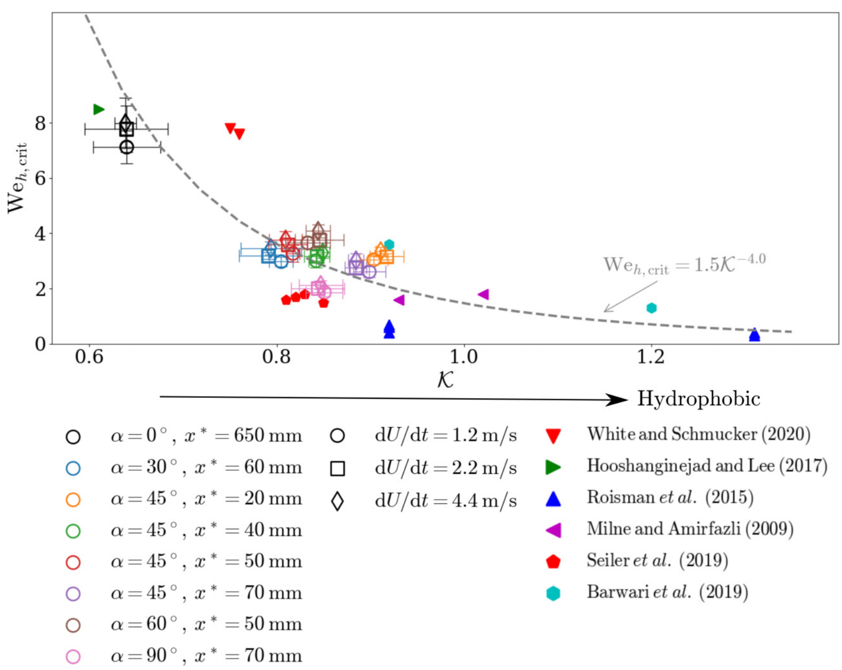

FIG. 11. Critical Weber number based on droplet height $\mathrm{We}_{h,\mathrm{crit}}$ as a function of volumetric shape factor $\mathcal{K}$ at depinning; the latter compares the droplet volume to that of an ellipsoid with base diameter L_b and height h.

do not change significantly around the time instant of depinning; thus, the measurement of h and L_b does not require identifying the exact time instant when droplet depins.

We note that, in the present study, the sessile droplet shapes were similar across all volumes, and as such the ratio L_{b_0}/A_0 is fixed. Consequently, the empirical relation proposed by [19] predicts the same critical depinning velocity for all cases explored herein. That is, in their study, which employed varying substrate-fluid combinations, surface hydrophilicity or hydrophobicity was the dominant factor determining critical depinning velocity. In the present work, although the initial droplet shape is fixed, differences in the incoming flow characteristics alters droplet shape prior to depinning due to nonsimilar aerodynamic loading across volumes, positions, and flow accelerations, which necessitates the aerodynamically motivated empirical relation in Eq. (5).

VI. CONCLUSION

The depinning characteristics of droplets on a flat plate subjected to wall-bounded shear flows formed by a flat plate boundary layer and impinging jets were presented. Critical droplet depinning conditions were investigated for varying initial droplet positions under three flow accelerations. Within the range of parameters investigated, critical velocities demonstrated a minor decrease with increasing droplet volume and decreasing flow acceleration. Notwithstanding the statistical significance, the impacts of droplet volume and flow acceleration are small compared with the effects of incoming flow orientation angle and relative submergence of the droplet in the wall jet or boundary layer. In addition, for the impinging jet configuration, the normally impinging jet produced a significantly lower critical velocity compared with the of other jet angles. This may possibly associate with the stronger droplet oscillations induced by flow events that are distinctive in impinging jets at high jet angles. However, it requires further investigation to fully unveil the potential influence of the transient flow events on droplet depinning.

Cast into dimensionless variables, the present study found the critical Weber number range for depinning due to a laminar boundary layer were comparable to values reported by White and Schmucker [20]. However, droplets subjected to impinging jets were found to depin at lower Weber numbers, and a wider range in this parameter was observed across different studies. The performed statistical analysis revealed an interrelation between several dimensionless groups, which was likely linked to the underlying effect of surface wettability on the droplet geometry at depinning. Consequently, it has been proposed to cast the closely correlated groups into a nondimensional volumetric shape factor, encapsulating droplet shape and related aspects of substrate wettability. Correlation analysis found critical Weber number to be strongly related to the introduced volumetric shape factor, and resulted in reasonable collapse of data from the present study and previous investigations. An empirical power-law relation was proposed for the critical Weber number, which can be employed to yield a simplified empirical formula for critical droplet depinning velocity. The proposed relation requires only fluid-substrate and droplet geometry information, which are much easier to obtain than accurate contact angle measurements, and coarse estimations may be obtained based on sessile droplet parameters.

ACKNOWLEDGMENT

The authors gratefully acknowledge the support of the Natural Sciences and Engineering Research Council (NSERC), Ontario Centres of Excellence (OCE), and Suncor Energy.

[1] E. B. White and J. A. Schmucker, A runback criterion for water drops in a turbulent accelerated boundary layer, J. Fluids Eng. **130**, 061302 (2008).

[2] S. Kulinich and M. Farzaneh, How wetting hysteresis influences ice adhesion strength on superhydrophobic surfaces, Langmuir **25**, 8854 (2009).

[3] S. Farhadi, M. Farzaneh, and S. Kulinich, Anti-icing performance of superhydrophobic surfaces, Appl. Surf. Sci. **257**, 6264 (2011).

[4] C. Antonini, M. Innocenti, T. Horn, M. Marengo, and A. Amirfazli, Understanding the effect of superhydrophobic coatings on energy reduction in anti-icing systems, Cold Reg. Sci. Technol. **67**, 58 (2011).

[5] S. Moghtadernejad, M. Tembely, M. Jadidi, N. Esmail, and A. Dolatabadi, Shear driven droplet shedding and coalescence on a superhydrophobic surface, Phys. Fluids **27**, 032106 (2015).

[6] H. Hu, B. Wang, K. Zhang, W. Lohry, and S. Zhang, Quantification of transient behavior of wind-driven surface droplet/rivulet flows using a digital fringe projection technique, J. Visualiz. **18**, 705 (2015).

[7] F. Y. Zhang, X. G. Yang, and C. Y. Wang, Liquid water removal from a polymer electrolyte fuel cell, J. Electrochem. Soc. **153**, A225 (2005).

[8] A. Theodorakakos, T. Ous, M. Gavaises, J. Nouri, N. Nikolopoulos, and H. Yanagihara, Dynamics of water droplets detached from porous surfaces of relevance to PEM fuel cells, J. Colloid Interface Sci. **300**, 673 (2006).

[9] A. Golpaygan and N. Ashgriz, Multiphase flow model to study channel flow dynamics of PEM fuel cells: Deformation and detachment of water droplets, Int. J. Comput. Fluid Dyn. **22**, 85 (2008).

[10] A. Esposito, A. D. Montello, Y. G. Guezennec, and C. Pianese, Experimental investigation of water droplet–air flow interaction in a non-reacting PEM fuel cell channel, J. Power Sources **195**, 2691 (2010).

[11] S. G. Kandlikar and M. E. Steinke, Contact angles and interface behavior during rapid evaporation of liquid on a heated surface, Int. J. Heat Mass Transfer **45**, 3771 (2002).

[12] A. D. Schleizer and R. T. Bonnecaze, Displacement of a two-dimensional immiscible droplet adhering to a wall in shear and pressure-driven flows, J. Fluid Mech. **383**, 29 (1999).

[13] S. Madani and A. Amirfazli, Oil drop shedding from solid substrates by a shearing liquid, Colloids Surf., A **441**, 796 (2014).

[14] V. Thoreau, B. Malki, G. Berthome, L. Boulange-Petermann, and J. Joud, Physico-chemical and dynamic study of oil-drop removal from bare and coated stainless-steel surfaces, J. Adhes. Sci. Technol. **20**, 1819 (2006).

[15] S. C. Fu, W. T. Leung, and C. Y. Chao, Detachment of droplets in a fully developed turbulent channel flow, Aerosol Sci. Technol. **48**, 916 (2014).

[16] W. T. Leung, S. C. Fu, and C. Y. Chao, Detachment of droplets by air jet impingement, Aerosol Sci. Technol. **51**, 467 (2017).

[17] E. Dussan, On the ability of drops to stick to surfaces of solids. 3. The influences of the motion of the surrounding fluid on dislodging drops, J. Fluid Mech. **174**, 381 (1987).

[18] H. Ding and P. D. Spelt, Onset of motion of a three-dimensional droplet on a wall in shear flow at moderate Reynolds numbers, J. Fluid Mech. **599**, 341 (2008).

[19] A. Milne and A. Amirfazli, Drop shedding by shear flow for hydrophilic to superhydrophobic surfaces, Langmuir **25**, 14155 (2009).

[20] E. B. White and J. A. Schmucker, Wind- and gravity-forced drop depinning, Phys. Rev. Fluids **6**, 023601 (2021).

[21] I. V. Roisman, A. Criscione, C. Tropea, D. K. Mandal, and A. Amirfazli, Dislodging a sessile drop by a high-Reynolds-number shear flow at subfreezing temperatures, Phys. Rev. E **92**, 023007 (2015).

[22] C. Extrand and A. Gent, Retention of liquid drops by solid surfaces, J. Colloid Interface Sci. **138**, 431 (1990).

[23] S. Taniguchi, H. Sakamoto, M. Kiya, and M. Arie, Time-averaged aerodynamic forces acting on a hemisphere immersed in a turbulent boundary, J. Wind Eng. Ind. Aerodyn. **9**, 257 (1982).

[24] M. Lamb, F. Brun, and B. Fuller, Direct measurements of lift and drag on shallowly submerged cobbles in steep streams: Implications for flow resistance and sediment transport, Water Resour. Res. **53**, 7607 (2017).

[25] P. Nardone and K. Koll, Velocity field and drag force measurements of a cube and a hemisphere mounted on an artificial bed surface roughness, E3S Web Conf. **40**, 05022 (2018).

[26] A. Milne, B. Defez, M. Cabrerizo-Vílchez, and A. Amirfazli, Understanding (sessile/constrained) bubble and drop oscillations, Adv. Colloid Interface Sci. **203**, 22 (2014).

[27] B. Barwari, S. Burgmann, A. Bechtold, M. Rohde, and U. Janoske, Experimental study of the onset of downstream motion of adhering droplets in turbulent shear flows, Exp. Therm. Fluid Sci. **109**, 109843 (2019).

[28] N. Lin, H. L. Reed, and W. S. Saric, Effect of leading edge geometry on boundary-layer receptivity to freestream sound, in *Stability, Transition and Turbulence*, edited by M. Y. Hussaini, A. Kumar, and C. L. Streett (Springer-Verlag, New York, 1992).

[29] X. Zhang, S. Yarusevych, and S. Peterson, Experimental investigation of flow development and coherent structures in normal and oblique impinging slot jets, Exp. Fluids **60**, 11 (2019).

[30] P. G. de Gennes, Wetting: statics and dynamics, Rev. Mod. Phys. **57**, 827 (1985).

[31] R. W. Schafer, What is a Savitzky-Golay filter?, IEEE Signal Process. Mag. **28**, 111 (2011).

[32] S. F. Chini and A. Amirfazli, A method for measuring contact angle of asymmetric and symmetric drops, Colloids Surf. A **388**, 29 (2011).

[33] N. Otsu, A threshold selection method from gray-level histograms, IEEE Trans. Syst. Man Cybern.: Syst. **9**, 62 (1979).

[34] J. Han and C. Moraga, The influence of the sigmoid function parameters on the speed of backpropagation learning, in *From Natural to Artificial Neural Computation*, edited by J. Mira and F. Sandoval, Lecture Notes in Computer Science Vol. 930 (Springer, Berlin, Heidelberg, 1995).

[35] V. Berejnov and R. E. Thorne, Effect of transient pinning on stability of drops sitting on an inclined plane, Phys. Rev. E **75**, 066308 (2007).

[36] A. Saal, P. M. Seiler, D. Rettenmaier, M. Ade, I. V. Roisman, R. Berger, H.-J. Butt, and C. Tropea, Shuffling gait motion of an aerodynamically driven wall-bound drop, Phys. Rev. Fluids **5**, 094006 (2020).

[37] J. Schmucker, Ph.D. thesis, Texas A&M University, 2012, https://oaktrust.library.tamu.edu/handle/1969.1/ETD-TAMU-2012-08-11530.

[38] X. Zhang, Ph.D. thesis, University of Waterloo, 2021, https://uwspace.uwaterloo.ca/handle/10012/16820.

[39] B. Everitt and A. Skrondal, *The Cambridge Dictionary of Statistics* (Cambridge University Press, Cambridge, 2002), Vol. 106.

[40] E. B. Dussan and R. T.-P. Chow, On the ability of drops or bubbles to stick to non-horizontal surfaces of solids, J. Fluid Mech. **137**, 1 (1983).

[41] P. M. Seiler, M. Gloerfeld, I. V. Roisman, and C. Tropea, Aerodynamically driven motion of a wall-bounded drop on a smooth solid substrate, Phys. Rev. Fluids **4**, 024001 (2019).

[42] F. White, *Fluid Mechanics* (Tata McGraw-Hill Education, 1979).

[43] A. Hooshanginejad and S. Lee, Droplet depinning in a wake, Phys. Rev. Fluids **2**, 031601(R) (2017).